NANO LETTERS

Letter

pubs.acs.org/NanoLett

Syringe Injectable Electronics: Precise Targeted Delivery with Quantitative Input/Output Connectivity

Guosong Hong,[†] Tian-Ming Fu,[†] Tao Zhou,[†] Thomas G. Schuhmann,[‡] Jinlin Huang,[†] and Charles M. Lieber*[,†,‡]

[†]Department of Chemistry and Chemical Biology and [‡]John A. Paulson School of Engineering and Applied Science, Harvard University, Cambridge, Massachusetts 02138, United States

Supporting Information

ABSTRACT: Syringe-injectable mesh electronics with tissue-like mechanical properties and open macroporous structures is an emerging powerful paradigm for mapping and modulating brain activity. Indeed, the ultraflexible macroporous structure has exhibited unprecedented minimal/noninvasiveness and the promotion of attractive interactions with neurons in chronic studies. These same structural features also pose new challenges and opportunities for precise targeted delivery in specific brain regions and quantitative input/output (I/O) connectivity needed for reliable electrical measurements. Here, we describe new results that address in a flexible manner both of these points. First, we have developed a controlled injection approach that maintains the extended mesh structure during the "blind" injection process, while also achieving targeted delivery with ca. 20 μm spatial precision. Optical and microcomputed tomography results from injections into tissue-like hydrogel, ex vivo brain tissue, and in vivo brains validate our basic approach and demonstrate its generality. Second, we present a general strategy to achieve up to 100% multichannel I/O connectivity using an automated conductive ink printing methodology to connect the mesh electronics and a flexible flat cable, which serves as the standard "plug-in" interface to measurement electronics. Studies of resistance versus printed line width were used to identify optimal conditions, and moreover, frequency-dependent noise measurements show that the flexible printing process yields values comparable to commercial flip-chip bonding technology. Our results address two key challenges faced by syringe-injectable electronics and thereby pave the way for facile in vivo applications of injectable mesh electronics as a general and powerful tool for long-term mapping and modulation of brain activity in fundamental neuroscience through therapeutic biomedical studies.

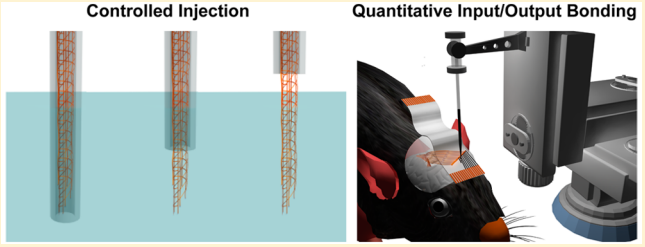

KEYWORDS: *Mesh electronics, ultraflexible brain probe, stereotaxic surgery, controlled injection, dense tissue/gel, high yield input/output connection, conductive ink printing*

Syringe-injectable electronics[1] represents a paradigm-shifting approach for seamless three-dimensional (3D) integration of electronics within man-made materials and living systems, for example, for in vivo interrogation and modulation of brain activity.[1−5] In particular, unlike traditional and relatively rigid implantable brain probes based on metal, silicon, and tens of micrometer thick polymer films,[6−10] the syringe-injectable electronics builds upon a submicron thickness macroporous mesh structure[11,12] with tissue-like mechanical properties.[1] Specifically, the syringe-injectable electronics have a bending stiffness 4−6 orders of magnitude smaller than traditional implantable probes,[1] mesh widths features on the 10 μm scale similar to neuronal soma and axons,[1] and ca. 90% free area structure that allows for facile neuronal interpenetration.[12] These unique structural and mechanical properties of syringe injectable electronics have yielded minimal damage and immune response post implantation in brain tissue as well as unprecedented attractive or "neurophilic" interactions with neurons thereby allowing for 3D interpenetration with intact neuronal networks.[1]

The ultraflexibility of the mesh electronics, which is central to the above advantages, also presents new challenges associated with the injection and input/output (I/O) connection processes. For example, during syringe-assisted injection into brain tissue the mesh electronics may crumple due to the extremely low bending stiffness of the structure. Such crumpling would displace the recording electrodes from expected stereotaxic injection coordinates and could thereby yield uncertainty in specific location from which signals are recorded. In addition, the small syringe needle diameters preclude injection of mesh electronics with prebonded I/O connectors, and the mesh thickness and flexibility make it incompatible with conventional semiconductor bonding methods such as wire-bonding or soldering. Although anisotropic conductive film (ACF) is a widely used approach for I/O bonding of flexible electronics,[1,10,13] the relatively high pressure and temperature required for ACF bonding can

Received: July 29, 2015
Revised: August 26, 2015
Published: August 28, 2015

DOI: 10.1021/acs.nanolett.5b02987
Nano Lett. 2015, 15, 6979−6984

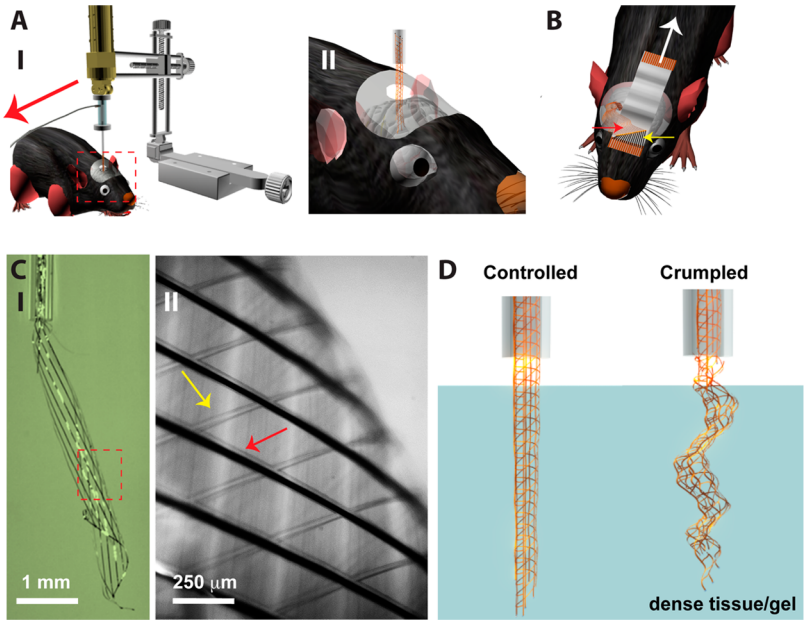

Figure 1. Overview of mesh electronics injection and I/O bonding. (A) Schematics (I) of the controlled injection setup for precise targeted delivery of mesh electronics into a live mouse brain using a syringe pump (red arrow indicates the direction of the catheter tubing connection to the syringe pump) and a stereotaxic frame equipped with a motorized linear translational stage (golden). (II) Zoom (dashed red box in I) of mouse head showing the extended mesh electronics inside the mouse brain after injection with needle outside the skull. (B) Schematic showing the I/O of the mesh electronics unfolded on a flexible flat cable (FFC); electrical connections between individual channels of the mesh (red arrow) and FFC are made by printed conductive ink (yellow arrow). The white arrow indicates the direction of the connection of the FFC cable to external instrumentation. (C, I) Image showing mesh electronics being injected from a glass needle into 1X PBS solution. The mesh electronics expands to a size larger than the needle ID (400 μm) in solution. Longitudinal metal interconnect lines are prominent in the image (due to good light reflection). (C, II) Magnified portion of mesh highlighted by red dashed box in I shows the full mesh structure. The red arrow highlights one of the longitudinal SU-8/metal interconnect/SU-8 elements, and the yellow arrow denotes a transverse SU-8 element (see Supporting Information Figure S2 for the structure of mesh electronics). (D) Schematics showing extended mesh electronics (left) and crumpled mesh electronics (right) post injection into dense tissue or gel.

damage the thin (<1 μm) and ultraflexible mesh electronics. In addition, postinjection unfolding of the ultraflexible mesh electronics on the flexible flat cables (FFCs) prior to interconnection can yield orientation and spatial distributions of I/O pads that cannot be bonded by ACF. Although these aforementioned challenges are not associated with conventional rigid probes, it is noteworthy that the ultraflexibility of syringe-injected electronics does not impose forces postinjection with respect to brain tissue and thus does not yield stresses at or motion with respect to targeted sites. Moreover, the intrinsically small and flexible nature of mesh electronics eliminates the bulky vertically protruding I/O interface typically associated with rigid brain probes and thus could benefit significantly chronic recording studies of animals.

The controlled injection elements of the stereotaxic surgery station used for in vivo brain probe implantation consist of a syringe pump and a motorized stereotaxic stage (Figure 1A, I and Supporting Information Figure S1A). The syringe pump typically injects 1X phosphate buffered solution (PBS) through a needle loaded with mesh electronics (Supporting Information Figure S1B) at a fixed volumetric rate (20−50 mL/h), while a motorized linear translation stage withdraws the "vertical" arm of the stereotaxic stage at a constant velocity (0.2−0.5 mm/s) that matches the ejection rate of the mesh electronics from the needle. In general, the fluid shear force that drives the mesh electronics out of needle must overcome the friction between the mesh electronics and the needle inner wall, and thus mesh structures with different designs and different needle inner diameters (IDs) will require different flow conditions to balance electronics injection and needle retraction rates necessary to achieve full extension of the mesh electronics (Figure 1A, II). The I/O bonding components of our setup, which are also compatible with the stereotaxic surgery station, consist of a motorized and computer-controlled microprinter (Supporting Information Figure S1A,C) that prints conductive ink in a programmable two-dimensional (2D) pattern that links I/O pads on the mesh electronics to corresponding channel lines of the FFC (Figure 1B), which then provides standard serial communication interface with the recording/control instrumentation.

The ultraflexible nature of the mesh electronics, which comprises the sensors, interconnects, and I/O pads (Supporting Information Figure S2), is readily evident upon injection into aqueous solution (Figure 1C), where the mesh spontaneously expands to a size substantially larger than injection needle and appears to "float" within the solution. In synthetic gels or dense tissue such as the brain, matching the mesh electronics injection and needle retraction rates is critical for achieving precise targeted delivery with a controlled and extended conformation (Figure 1D, left) versus, for example, a crumpled conformation (Figure 1D, right), which results from the needle being retracted more slowly than the mesh injection rate. The latter crumpled configuration yields poorly defined sensor device positions.

A general attribute of syringe injection is the ability to deliver materials to hidden or opaque regions, such as tissue within the brain, in a minimally invasive manner. As discussed above for the specific case of syringe injection of mesh electronics, it is

DOI: 10.1021/acs.nanolett.5b02987
Nano Lett. 2015, 15, 6979−6984

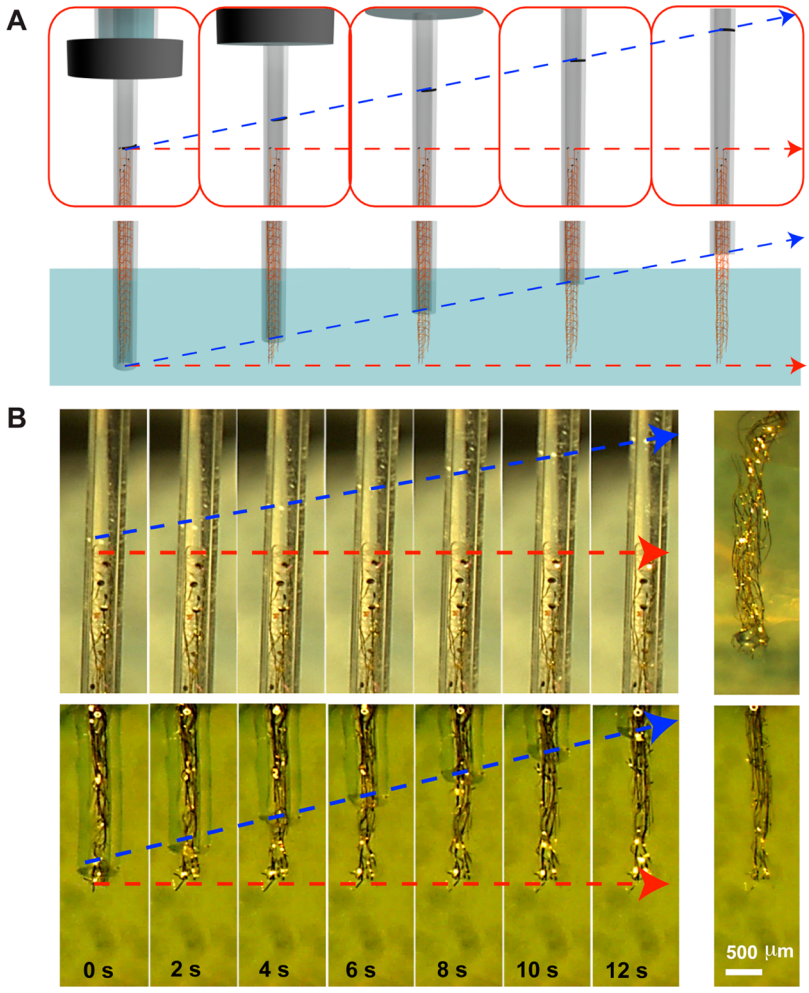

Figure 2. FoV controlled delivery of mesh electronics. (A) Schematics illustrating controlled injection by the FoV method. The top row shows the mesh I/O pads remain stationary (red dashed arrow) within the FoV (red box) while the needle is retracted upward (blue dashed arrow following the black dash marked on the needle's exterior), resulting in fully extended mesh electronics structure inside the injected medium during needle withdrawal (bottom row). (B) Photographs showing the FoV injection process into 0.5% agarose hydrogel. The top row shows the needle moving upward (blue dashed arrow) with the mesh I/O pads remaining stationary (red dashed arrow) in the FoV. The bottom series of images recorded at same time points shows the same injection process of an independent mesh structure obtained at the end of the mesh electronics in the gel. Images of the lower part of the mesh electronics in the agarose hydrogel post injection are shown in the far right panels for each experiment.

important to have visual guidance and feedback to match mesh injection/needle retraction rates to ensure the mesh electronics is delivered into a targeted brain region with extended conformation. Because direct visualization of mesh electronics inside an opaque material such as the brain cannot be carried out during injection, we devised a general method based on visualization and real-time tracking of the upper I/O end of the mesh electronics in the field of view (FoV) of an eyepiece camera (Figure 2A). The FoV method dictates that if the mesh electronics remains fully extended along the longitudinal direction during the injection process without displacement then the absolute spatial location of the mesh electronics remains the same and an image of the upper end of the mesh should be fixed in the camera FoV. In other words, precisely targeted delivery of the mesh sensor electrodes can be achieved by ensuring that the mesh stays stationary in the FoV while the needle moves upward in the FoV (Figure 2A, top). Correspondingly, although the bottom end of the mesh electronics remains invisible to the operator, the mesh remains stationary in the injected medium with sensing electrodes at the predefined target positions (Figure 2A, bottom), while the needle is retracted.

The capabilities of the FoV method were explored by injecting mesh electronics in 0.5% agarose hydrogel. This composition of hydrogel is a good mimic of brain tissue since both the Young's modulus and shear modulus are similar to those of brain tissue.[14−18] In addition, the optical transparency of the hydrogel allows for direct imaging of injected mesh. In experiments carried out with fluid injection rates of 20−50 mL/h and needle retraction speeds of 0.2−0.5 mm/s, it was possible to meet the stationary FoV conditions (top, Figure 2B; Supporting Information Video S1) as evidenced by the stationary I/O pads (red dashed arrow, top, Figure 2B) as the needle was withdrawn at a constant speed (blue dashed arrow). A video of the injection (Supporting Information Video S1) highlights the dynamic balance of the injection/retraction rates for the full length of the process. An independent balanced injection/retraction rate experiment with the camera set to image the mesh injected in the hydrogel (bottom, Figure 2B; Supporting Information Video S2) reveals that the bottom edge of the mesh electronics remains stationary (red dashed

DOI: 10.1021/acs.nanolett.5b02987
Nano Lett. 2015, 15, 6979−6984

arrow, bottom, Figure 2B) as the needle was withdrawn upward (blue dashed arrow). A video of the injection (Supporting Information Video S2) spotlights the good stability of the mesh end during this dynamic injection/retraction process. Last, both injections resulted in fully extended mesh structures in the longitudinal direction at the completion of the injection process (far right image panels, Figure 2B).

Analyses of the above results and additional experiments highlight several important points. First, the total volume of liquid delivered into the hydrogel during injection of an ca. 5 mm length of mesh electronics is typically 10−100 μL. Significantly, this volume is similar to the volume of liquid introduced during intracranial injection of virus vectors and enzymes, 1−100 μL.[19−23] Second, the final positioning precision of the mesh electronics in hydrogel measured during the injection process from the camera images is ca. 20 μm from the original target coordinates at t = 0 s (see Materials and Methods in the Supporting Information for details). This relatively small positioning uncertainty suggests that our FoV injection approach can achieve precise targeted delivery of mesh electronics with tolerance smaller than the thickness of key subfields/layers of the mouse brain: for example, the CA-1 subfield of the hippocampus is ca. 620 μm thick, CA-3 subfield is ca. 230 μm thick,[24] and cortical layer V is ca. 300 μm thick.[25] Third, the importance of matching mesh injection/needle retraction rates was confirmed by control experiments (Supporting Information Figure S3). Specifically, when the rate of needle retraction was slower than needed to exert sufficient kinetic friction force and balance the expulsion force due to fluid injection, we observed crumpling of the ultraflexible mesh electronics (Supporting Information Figure S3A), and when the needle retraction rate was faster and thus exerted larger kinetic friction force than the expulsion force, the mesh was displaced upward from the initial targeted position during injection (Supporting Information Figure S3B). Last, studies of FoV injection into tissue-like hydrogel for angles up to 45° off vertical (Supporting Information Figure S4) demonstrate similar targeting capabilities as vertical injection and thus show that controlled targeted delivery to brain regions that are typically difficult to access using vertical injection alone[26] will be accessible with our approach.

We have applied the FoV method to investigate the potential for controlled injection of mesh electronics into opaque ex vivo fixed brain tissue and in vivo live mouse brain. A schematic for the in vivo injection (Figure 3A) emphasizes the general experimental protocol of making two or more mesh injections at distinct sites prior to analysis. We injected four mesh electronics samples at different sites in the ex vivo brain tissue, where three injections were using our balanced FoV method and one was injected manually. Because the opaque nature of the brain tissue precluded direct optical imaging, we used microcomputed tomography (micro-CT; see Materials and Methods in the Supporting Information) to visualize the mesh electronics structure postinjection, where the high X-ray attenuation contrast of metal interconnects compared to tissue allows for clear contrast of the mesh electronics. A 3D reconstruction of the ex vivo mouse brain following the above mesh injections (Figure 3B) reveals several key points. First, the mesh electronics injected by the balanced FoV approach exhibited the desired fully extended morphology (yellow arrows). Second, the manually injected sample showed a crumpled structure (blue arrow) in the brain tissue. We note that it was not possible to distinguish these differences in internal morphology by optical visualization of the exterior of the brain (Figure 3B inset) as all injections produced minimal visual damage/bleeding.

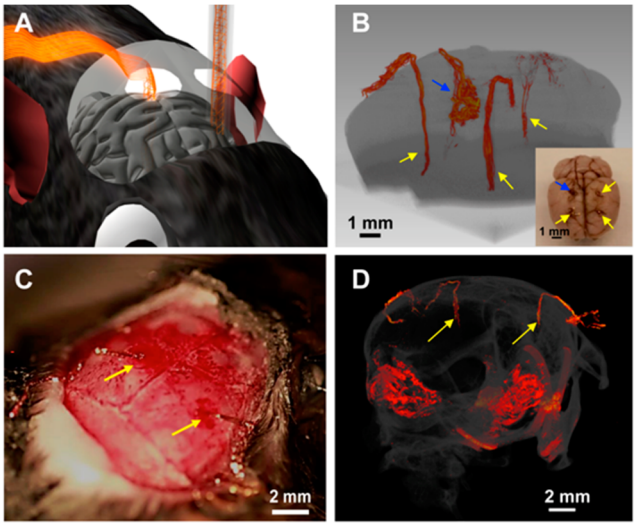

Figure 3. Blind injection of mesh electronics using the FoV method into brain tissue. (A) Schematic showing blind injection of multiple mesh electronics samples into the brain of a live mouse. The mesh electronics on the left is already injected with its I/O (left) unfolded on the skull, while the mesh electronics on the right is in the middle of the injection process. (B) Micro-CT reconstructed image of an ex vivo mouse brain (gray) blind-injected with 4 mesh electronics samples (red). Inset is white-light optical image of the brain surface. Blue arrows indicate the mesh electronics injected manually, and yellow arrows indicate the mesh electronics delivered via the balanced FoV controlled injection process. (C) White-light optical photograph showing live mouse skull following blind injection of two mesh electronics samples (indicated by yellow arrows), where both were injected using the balanced FoV controlled injection method. (D) Micro-CT reconstructed image of the same mouse head in (C) showing the extended mesh electronics structures (red, indicated by yellow arrows) inside the skull (gray).

In addition, in vivo injection of two mesh electronic structures into the left and right cerebral hemispheres was carried out using the balanced FoV controlled injection setup under a stereotaxic stage and through predrilled holes in the cranial bone (Figure 3C; see Materials and Methods in the Supporting Information for stereotaxic coordinates of the two injections). Analysis of the 3D reconstructed micro-CT obtained postinjection (Figure 3D) demonstrates the fully extended mesh morphology positioned at the chosen brain coordinates for both injected mesh electronics samples. The capability to achieve well-controlled mesh electronics injections into ex vivo whole mouse brains and in vivo live mouse brains highlight several key points. First, synchronized and balanced mesh injection and needle retraction, which are difficult to achieve in manual injections, enable the mesh electronics to be extended and kept stationary with respect to the optically opaque brain tissue. Second, micro-CT imaging verified the effectiveness of the FoV method by proving the extended morphology of injected mesh electronics and the precise positioning within the brain using the stereotaxic stage.

Last, we have achieved quantitative I/O connectivity of the multiplexed mesh electronics through an automated conductive ink printing method (Figure 4A). The conductive ink used in our work was comprised of surfactant-solubilized carbon nanotubes (CNT) in an aqueous solution (see Materials and

DOI: 10.1021/acs.nanolett.5b02987
Nano Lett. 2015, 15, 6979−6984

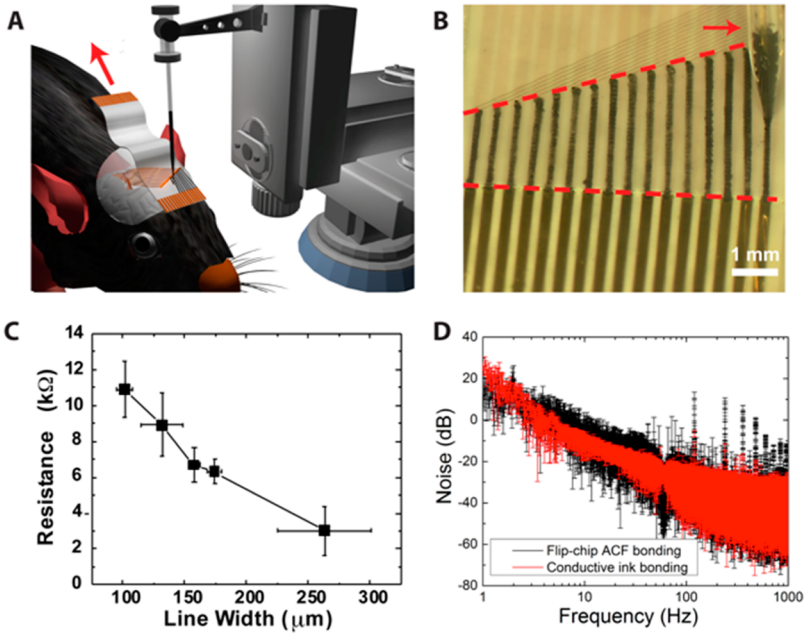

Figure 4. Conductive ink printing for I/O connectivity. (A) Schematic showing the automated conductive ink printing approach used to achieve high-yield I/O bonding of the mesh electronics to an FFC cable. The red arrow highlights the connection from the FFC to external recording instrumentation. (B) White-light optical image showing all 16 channels in the mesh electronics (lined-up along the top red dashed line) bonded to the 16 metal lines of the FFC cable (lower red dashed line) by the conductive ink printing method, where the printed CNT lines are between the two red dashed lines. The red arrow indicates the glass capillary tube loaded with conductive ink. (C) Resistance of conductive ink printed lines as a function of line width. All lines are printed to a total length of 5 mm. (D) Noise spectra for mesh electronics sensor electrodes immersed in 1X PBS solution and recorded following bonding of mesh electronics I/O by standard ACF bonding (black curve) and our conductive ink printing (red curve) methods.

Methods in the Supporting Information for detailed information). The CNT suspension was loaded into a glass capillary tube with tapered tip (ID = 150 μm) and subsequently printed as droplets on the FFC surface (Figure 4B; Supporting Information Movie S3). For a 16-channel mesh electronics structure with recording electrodes injected into dense tissue as described above, the I/O pads at the other end of the mesh structure (Supporting Information Figure S2) were unfolded on the surface of an FFC interface cable to expose the electrical connection pads for all 16 channels of the mesh electronics. The spatial coordinates of the mesh I/O pads and all FFC electrodes were taken as inputs into the automated micro-printer, which then computed the shortest path for each connection and carried out conductive ink printing to make electrical connections between all available channels in the mesh and the FFC with a bonding yield of 100% (Figure 4B). Another example in Supporting Information Figure S5 shows imperfectly unfolded mesh I/O pads, which are not lined up in a straight line but in a curve (red dashed line, Supporting Information Figure S5) with varying pitch distance between neighboring I/O pads (blue labels, Supporting Information Figure S5). This nonideal I/O alignment cannot be bonded by ACF but are readily connected in 100% yield by our printing method, thus highlighting the clear advantage compared to the ACF method. The typical time scale for unfolding the I/O pads on the FFC cable is ca. 10 min and that for completing the 16-channel I/O connection through conductive ink printing is ca. 30 min.

The resistance of the printed CNT lines was characterized using four-point measurements as a function of line width for a fixed length of 5 mm, where the 5 mm limit was longer than lines typically used in practice. These results (Figure 4C) illuminate several key points. First, the resistance of the printed CNT lines decreased as a function of line width with fixed length as expected with an estimated resistivity of $(1.04 \pm 0.15) \times 10^{-2}$ Ω·m. Second, from these data we estimate that a typical CNT line with average width of ~150 μm and average length of ~3.5 mm will have a resistance of ca. 4.2 kΩ, which is much smaller than the typical interface impedance, 100 -- 1000 kΩ) between metal sensing electrodes and physiological solution. To further validate the utility of the conductive ink printing method, we compared the noise spectra recorded from mesh electronics sensor elements following bonding by either (1) standard flip-chip ACF bonding, which is the standard method for flexible electronics[1,10,13] and (2) our new conductive ink printing method. Notably, these data shown in Figure 4D exhibit comparable noise-frequency dependence and thus validate our new approach. We are currently using this bonding method to carry out long-term chronic recording measurements in awake mice.

In conclusion, we have reported controlled injection and conductive ink printing techniques to address the challenges associated with the ultraflexible nature of syringe-injectable electronics. Controlled injection was achieved by balancing the electronics injection and the needle retraction rates, resulting in a mesh electronics structure that remains stationary and fully extended in the dense medium, thus allowing for targeted delivery of mesh electronics in any specific brain region with ca. 20 μm targeting precision. Optical and micro-CT imaging results from injections of mesh electronics into tissue-like hydrogel, ex vivo brain tissue and in vivo brains demonstrate the FoV controlled injection as a general method to achieve precise targeted delivery of mesh electronics without crumpling or displacement during injection. In addition, up to 100% I/O

DOI: 10.1021/acs.nanolett.5b02987
Nano Lett. 2015, 15, 6979−6984

connectivity was demonstrated using computer-controlled hands-free conductive ink printing, which allows for customized patterns to accommodate different orientations of the mesh electronics I/O pads and pre-positions of FFC interface. Notably, frequency-dependent noise measurements show that our conductive ink printing process is comparable to commercial flip-chip bonding technology. These advances in controlled injection and I/O bonding of the mesh electronics together with previous studies showing minimal or the absence of chronic tissue response[1] now open up many opportunities for chronic brain recording using injectable electronics, including elucidating changes in neural circuits as a function of learning[27,28] and neuropathologies.[29,30]

■ ASSOCIATED CONTENT

Supporting Information

The Supporting Information is available free of charge on the ACS Publications website at DOI: 10.1021/acs.nanolett.5b02987.

Materials and Methods, Supplementary Figures S1−S5, Supplementary Video Captions S1−S3, and Supplementary References. (PDF)

Field of view (FoV) controlled injection into hydrogel. (AVI)

Controlled injection obtained by monitoring the mesh end inside the hydrogel. (AVI)

Automated conductive ink printing of I/O connections. (AVI)

■ AUTHOR INFORMATION

Corresponding Author

*E-mail: cml@cmliris.harvard.edu.

Author Contributions

G.H. and T.-M.F. contributed equally to this work.

Notes

The authors declare no competing financial interest.

■ ACKNOWLEDGMENTS

We thank Dr. Jia Liu for helpful discussions. C.M.L. acknowledges support of this work by the Air Force Office of Scientific Research, the Star Family, and Fidelity Biosciences Funds.

■ REFERENCES

(1) Liu, J.; Fu, T.-M.; Cheng, Z. G.; Hong, G. S.; Zhou, T.; Jin, L. H.; Duvvuri, M.; Jiang, Z.; Kruskal, P.; Xie, C.; Suo, Z. G.; Fang, Y.; Lieber, C. M. *Nat. Nanotechnol.* **2015**, *10*, 629−636.

(2) Kim, D.-H.; Lee, Y. *Nat. Nanotechnol.* **2015**, *10*, 570−571.

(3) Gibney, E. *Nature* **2015**, *522*, 137−138.

(4) Vogt, N. *Nat. Methods* **2015**, *12*, 702−703.

(5) Jarchum, I. *Nat. Biotechnol.* **2015**, *33*, 830−830.

(6) Schwarz, D. A.; Lebedev, M. A.; Hanson, T. L.; Dimitrov, D. F.; Lehew, G.; Meloy, J.; Rajangam, S.; Subramanian, V.; Ifft, P. J.; Li, Z.; Ramakrishnan, A.; Tate, A.; Zhuang, K. Z.; Nicolelis, M. A. L. *Nat. Methods* **2014**, *11*, 670−676.

(7) Berenyi, A.; Somogyvari, Z.; Nagy, A. J.; Roux, L.; Long, J. D.; Fujisawa, S.; Stark, E.; Leonardo, A.; Harris, T. D.; Buzsaki, G. *J. Neurophysiol.* **2014**, *111*, 1132−1149.

(8) Khodagholy, D.; Gelinas, J. N.; Thesen, T.; Doyle, W.; Devinsky, O.; Malliaras, G. G.; Buzsaki, G. *Nat. Neurosci.* **2014**, *18*, 310−315.

(9) Kim, T. I.; McCall, J. G.; Jung, Y. H.; Huang, X.; Siuda, E. R.; Li, Y. H.; Song, J. Z.; Song, Y. M.; Pao, H. A.; Kim, R. H.; Lu, C. F.; Lee, S. D.; Song, I. S.; Shin, G.; Al-Hasani, R.; et al. *Science* **2013**, *340*, 211−216.

(10) Kim, D. H.; Viventi, J.; Amsden, J. J.; Xiao, J. L.; Vigeland, L.; Kim, Y. S.; Blanco, J. A.; Panilaitis, B.; Frechette, E. S.; Contreras, D.; Kaplan, D. L.; Omenetto, F. G.; Huang, Y. G.; Hwang, K. C.; Zakin, M. R.; et al. *Nat. Mater.* **2010**, *9*, 511−517.

(11) Tian, B. Z.; Liu, J.; Dvir, T.; Jin, L. H.; Tsui, J. H.; Qing, Q.; Suo, Z. G.; Langer, R.; Kohane, D. S.; Lieber, C. M. *Nat. Mater.* **2012**, *11*, 986−994.

(12) Liu, J.; Xie, C.; Dai, X. C.; Jin, L. H.; Zhou, W.; Lieber, C. M. *Proc. Natl. Acad. Sci. U. S. A.* **2013**, *110*, 6694−6699.

(13) Kim, D. H.; Lu, N. S.; Ghaffari, R.; Kim, Y. S.; Lee, S. P.; Xu, L. Z.; Wu, J. A.; Kim, R. H.; Song, J. Z.; Liu, Z. J.; Viventi, J.; de Graff, B.; Elolampi, B.; Mansour, M.; Slepian, M. J.; et al. *Nat. Mater.* **2011**, *10*, 316−323.

(14) Chen, Z. J.; Gillies, G. T.; Broaddus, W. C.; Prabhu, S. S.; Fillmore, H.; Mitchell, R. M.; Corwin, F. D.; Fatouros, P. P. *J. Neurosurg.* **2004**, *101*, 314−322.

(15) Ahearne, M.; Yang, Y.; El Haj, A. J.; Then, K. Y.; Liu, K. K. *J. R. Soc., Interface* **2005**, *2*, 455−463.

(16) Chen, X. M.; Sarntinoranont, M. *Ann. Biomed. Eng.* **2007**, *35*, 2145−2158.

(17) Deepthi, R.; Bhargavi, R.; Jagadeesh, K.; Vijaya, M. S. *SAS Tech Journal* **2010**, *9*, 27−30.

(18) Pervin, F.; Chen, W. W., Mechanically similar gel simulants for brain tissues. In *Dynamic Behavior of Materials*; Springer: New York, 2011; Vol. *1*, pp 9−13.

(19) Zhang, F.; Gradinaru, V.; Adamantidis, A. R.; Durand, R.; Airan, R. D.; de Lecea, L.; Deisseroth, K. *Nat. Protoc.* **2010**, *5*, 439−456.

(20) Xue, M. Z.; Hollenberg, M. D.; Yong, V. W. *J. Neurosci.* **2006**, *26*, 10281−10291.

(21) Brian, J. E.; Moore, S. A.; Faraci, F. M. *Stroke* **1998**, *29*, 2600−2605.

(22) Shen, J. *Factors Influencing Topotecan CNS Penetration in Mouse Models*; ProQuest: Ann Arbor, MI, 2008.

(23) Huang, C. C.; Liu, C. C.; Wang, S. T.; Chang, Y. C.; Yang, H. B.; Yeh, T. F. *Pediatr. Res.* **1999**, *45*, 120−127.

(24) Lein, E. S.; Hawrylycz, M. J.; Ao, N.; Ayres, M.; Bensinger, A.; Bernard, A.; Boe, A. F.; Boguski, M. S.; Brockway, K. S.; Byrnes, E. J.; Chen, L.; Chen, L.; Chen, T. M.; Chin, M. C.; Chong, J.; et al. *Nature* **2007**, *445*, 168−176.

(25) Hattox, A. M.; Nelson, S. B. *J. Neurophysiol.* **2007**, *98*, 3330−3340.

(26) Afif, A.; Minotti, L.; Kahane, P.; Hoffmann, D. *Epilepsia* **2010**, *51*, 2305−2315.

(27) Zhang, Y.; Cudmore, R. H.; Lin, D. T.; Linden, D. J.; Huganir, R. L. *Nat. Neurosci.* **2015**, *18*, 402−407.

(28) Ho, V. M.; Lee, J. A.; Martin, K. C. *Science* **2011**, *334*, 623−628.

(29) Viventi, J.; Kim, D. H.; Vigeland, L.; Frechette, E. S.; Blanco, J. A.; Kim, Y. S.; Avrin, A. E.; Tiruvadi, V. R.; Hwang, S. W.; Vanleer, A. C.; Wulsin, D. F.; Davis, K.; Gelber, C. E.; Palmer, L.; Van der Spiegel, J.; et al. *Nat. Neurosci.* **2011**, *14*, 1599−U138.

(30) Famm, K.; Litt, B.; Tracey, K. J.; Boyden, E. S.; Slaoui, M. *Nature* **2013**, *496*, 159−161.

DOI: 10.1021/acs.nanolett.5b02987
Nano Lett. 2015, 15, 6979−6984